Electronic Supplementary Material (ESI) for Nanoscale.
This journal is © The Royal Society of Chemistry 2022

Electronic Supplementary Information

Cubic versus Hexagonal – Phase, Size and Morphology Effects on the Photoluminescence Quantum Yield of NaGdF$_4$:Er^{3+}/Yb^{3+} Upconverting Nanoparticles

Marta Quintanilla,*[a,i] Eva Hemmer,*[a,j] Jose Marques-Hueso, [b] Shadi Rohani,[a] Giacomo Lucchini,[e] M. Wang,[a] Reza R. Zamani,[c] Vladimir Roddatis,[d,k] Adolfo Speghini,[e] Bryce S. Richards[f, g] and Fiorenzo Vetrone*[a,h]

a. Institut National de la Recherche Scientifique, Centre Énergie, Matériaux et Télécommunications (INRS - EMT), Université du Québec, 1650 Boul. Lionel-Boulet, Varennes, QC, J3X 1P7 (Canada)

b. Heriot-Watt University, Institute of Sensors, Signals and Systems. Edinburgh, EH14 4AS Scotland (United Kingdom)

c. Georg-August-Universität Göttingen, IV. Physikalisches Institut, Friedrich-Hund-Platz 1, 37077 Göttingen (Germany)

d. Georg-August-Universität Göttingen, Institut für Materialphysik, Friedrich-Hund-Platz 1, 37077 Göttingen (Germany)

e. Nanomaterials Research Group, Dipartimento di Biotecnologie, Università di Verona and INSTM, UdR Berona, Strada di Grazie 15, I-37134 Verona (Italy)

f. Karlsruhe Institute of Technology (KIT), Institute of Microstructure Technology, Hermann-von-Helmholtz-Platz 1, 76344 Eggenstein-Leopoldshafen (Germany).

g. Karlsruhe Institute of Technology (KIT), Light Technology Institute, Engesserstrasse 13, 76131 Karlsruhe (Germany)

h. Centre Québécois sur les Matériaux Fonctionnels (CQMF)/Québec Centre for Advanced Materials (QCAM), INRS - EMT, Varennes, QC, J3X 1P7 (Canada).

i. Universidad Autónoma de Madrid, Materials Physics Department. Avda. Francisco Tomás y Valiente 7. 28049 Madrid (Spain).

j. University of Ottawa, Department of Chemistry and Biomolecular Sciences, 10 Marie-Curie, Ottawa, ON, K1N 6N5 (Canada)

k. GFZ German Research Centre for Geosciences, Telegrafenberg, 14473 Potsdam (Germany).

*Corresponding authors:
Prof. Vetrone (fiorenzo.vetrone@inrs.ca)
Prof. Hemmer (ehemmer@uottawa.ca)
Dr. Quintanilla (marta.quintanilla@uam.es)

Contents:

S1. Synthesis of Upconverting Nanoparticles

Materials. Starting materials including the Ln^{3+} oxides (Gd_2O_3, REacton®, 99.999 %, < 10 µm powder; Yb_2O_3, REacton®, 99.998 %, powder; Er_2O_3, REacton®, 99.99 %, powder, Alfa Aesar, Ward Hill, USA), sodium trifluoroacetate (CF_3COONa, 98 %, Sigma Aldrich, St. Louis, USA), trifluoroacetic acid (CF_3COOH, 99 %, Alfa Aesar, Ward Hill, USA), 1-octadecene ($CH_3(CH_2)_{15}CH=CH_2$, tech. 90 %, Alfa Aesar, Ward Hill, USA), and oleic acid (OA, $CH_3(CH_2)_7CH=CH(CH_2)_7COOH$, tech. 90 %, Alfa Aesar, Ward Hill, USA) were used without further purification. The synthesis of the UCNPs was carried out in a well-ventilated fume hood following a thermal decomposition process described previously.[1-3]

Preparation of lanthanide trifluoroacetate precursors. In a typical synthesis of the precursor used in the preparation of $NaGdF_4:Er^{3+}/Yb^{3+}$, 0.975 mmol of Gd_2O_3 (353.4 mg), 0.25 mmol of Yb_2O_3 (98.5 mg, 20 mol% doping concentration), and 0.025 mmol of Er_2O_3 (9.6 mg, 2 mol% doping concentration) were mixed with 5 mL of distilled water and 5 mL of trifluoroacetic acid in a 50 mL three-neck round-bottom flask. The mixture was refluxed under magnetic stirring at 80 °C for few hours until a clear solution was obtained. The temperature was then lowered to 60 °C to slowly evaporate residual water and trifluoroacetic acid overnight. The precursor was obtained as a dry, white solid.

Synthesis of upconverting nanoparticles (UCNPs). For the preparation of $NaGdF_4$ UCNPs doped with 2 mol% Er^{3+} and 20 mol% Yb^{3+}, 12.5 mL each of the high boiling solvent 1-octadecene and of the coordinating oleic acid (OA) were mixed in the reaction vessel (100 mL three-neck round-bottom flask) and degassed for 30 min at 150 °C under vacuum and magnetic stirring. Meanwhile, 2.5 mmol of sodium trifluoroacetate (340 mg) as well as 7.5 mL each of 1-octadecene and OA were added to the prepared precursor. The mixture was degassed at 125 °C under vacuum and magnetic stirring. Subsequently, the reaction vessel containing the degassed 1-octadecene and OA was heated under gentle argon flow to the required injection temperature (300 or 315 °C, Table S1). The hot precursor solution was then added dropwise to the reaction vessel using a syringe and pump system (Harvard Apparatus, Pump 11 Elite; injection rate: 1-2 mL/min; see Table S1 for further details). Following injection, the solution was maintained at the reaction temperature and stirred during the aging of the UCNPs under argon flow (reaction temperatures and time are also provided in Table S1). For all samples, the solution obtained after aging was allowed to cool to room temperature. The resultant UCNPs were precipitated by addition of ethanol and recovered by centrifugation at 5500 rpm for 15 min. The obtained white powder was washed twice with a mixture of hexane and ethanol (1:4 v/v) followed by centrifugation. The resultant oleate-capped UCNPs were finally redispersed in hexane for storage. All reaction parameters as well as sample names are summarized in Table S1. It must be noted that UCNPs of similar size can exhibit different V/S ratios due to different shape and morphology (e.g., in case of α-22 and α-26, a different degree of truncation resulted in different V/S ratios).

Table S1. Overview of synthesis conditions, host materials, assigned sample names and particle dimensions (as measured from TEM images). Note that the dimensions offered for each sample depend on the shape of the UCNPs (sphere, truncated cube, hexagonal plate). A detailed description of each dimension is provided in **Table S3**.

Phase	Sample	Injection Rate (mL/min)	Injection Temp. (°C)	Aging Temp. (°C)	Aging Time (min)	Shape	Particle Dimensions (nm)		S/V (nm^{-1})
							Diameter 2*r*	Thickness t	
β-NaGdF$_4$	β-14	2.00	315	315	60	Sphere	14 ± 1	-	0.43
	β-15	1.25	315	315	30	Sphere	15 ± 1	-	0.40
	β-23	1.50	315	315	60	Hexagon	23 ± 1	20 ± 1	0.30
	β-35	1.00	315	315	60	Hexagon	35 ± 1	23 ± 2	0.22
	β-37	1.50	320	320	60	Hexagon	37 ± 2	22 ± 1	0.21
	β-50	1.00	315	315	60	Hexagon	50 ± 1	29 ± 2	0.16
	β-98	1.20	315	315	60	Hexagon	98 ± 2	51 ± 4	0.08

Phase	Sample	Injection Rate (mL/min)	Injection Temp. (° C)	Aging Temp. (° C)	Aging Time (min)	Shape	Particle Dimensions (nm)		S/V (nm^{-1})
							Diameter 2*r*	Side Length 2*d*	
α-NaGdF$_4$	α-15	1.50	315	315	60	Sphere	15 ± 2	-	0.40
	α-22	1.75	315	315	30	Truncated Cube	-	22 ± 2	0.25
	α-26	2.00	315	315	60	Truncated Cube	-	26 ± 2	0.21
	α-29	1.50	310	310	60	Truncated Cube	-	29 ± 2	0.20

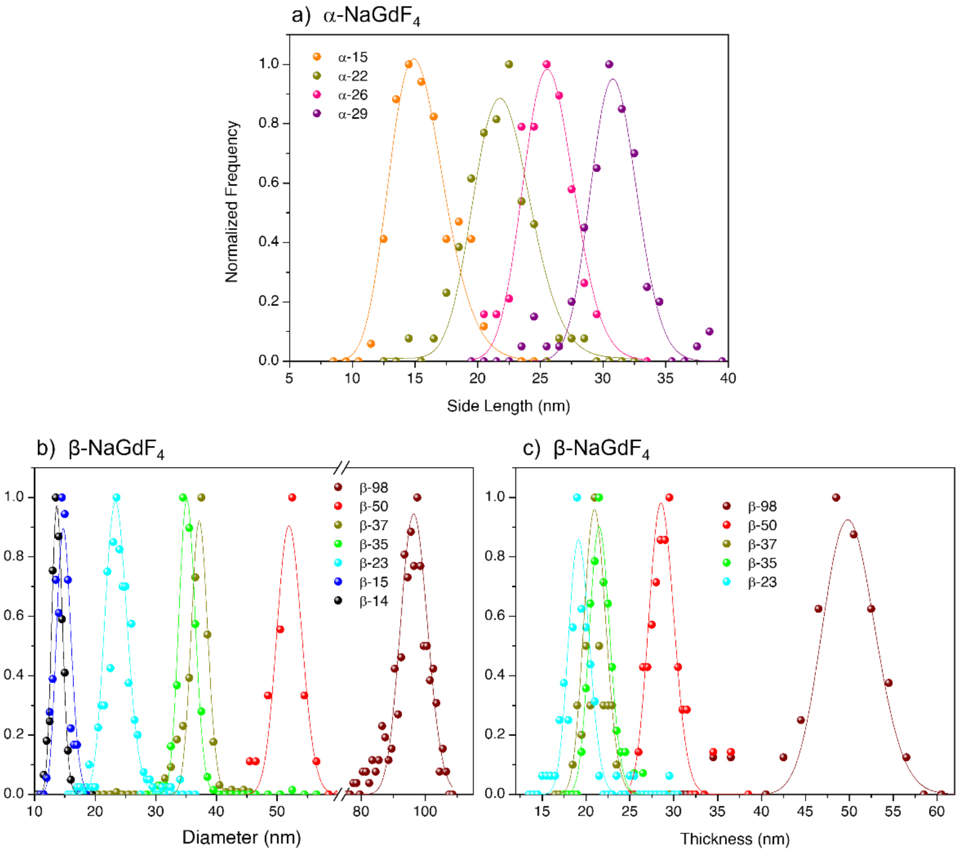

Figure S1. Size distribution obtained from TEM images, including a) the side of the α-phase particles (except for α-15, which is spherical and thus, its diameter was determined), b) diameter and c) thickness of the β-phase particles shaped as hexagonal plates.

S2. Characterization Techniques

Morphological and structural characterization. The crystalline phase of the samples was determined by powder X-ray diffraction (XRD) with a Bruker D8 Advance Diffractometer using CuKα radiation. The obtained XRD patterns were analysed with the help of the Bruker Diffrac Plus EVA software allowing for the phase assignment as well as the calculation of the lattice parameters in each sample. The morphology and size distributions of the obtained powders were investigated by transmission electron microscopy (TEM) (Philips CM200 High-Resolution TEM). The average particle size of all samples under investigation was determined based on measurements of a few hundred UCNPs with the help of the software ImageJ. The crystal structure, more detailed morphology, and faceting of the UCNPs were further studied by high-resolution transmission electron microscopy (HRTEM), and atomic resolution high-angle annular dark-field (HAADF) imaging in scanning transmission electron microscopy (STEM) mode. These experiments were performed on a Tecnai Titan 80-300 ETEM, operated at 300 kV, and equipped with a Cs image corrector and a monochromator. 3D atomic models of the UCNPs were created by using Rhodius software package.[4] The created models were utilized for linear STEM image simulations by STEM_CELL software tool.[5, 6] Equations listed in Table S3 (see Section S5) were applied to estimate the surface and volume of the various morphologies.

Elemental and surface analysis. The elemental composition of NaGdF4:Er3+/Yb3+ UCNPs was analysed by inductively coupled plasma - optical emission spectrometry (ICP-OES, Model 5100, Agilent Technologies). For each sample, 20 mg of $NaGdF_4:Er^{3+}/Yb^{3+}$ was digested in 10 ml of 5% aqua regia at 50 °C for 12 h, until the solution was clear. ICP-OES measurements were subsequently performed on the resultant solutions and the concentrations of Gd^{3+} and Na^+ ions were determined through comparison with standard solutions (concentrations: 0, 0.1, 0.2, 0.5, 1, 2, 5, 10, and 20 ppm). The selected wavelengths to detect each element were 589.592 nm for Na^+ and 342.246 nm for Gd^{3+}. In order to determine the amount of OA on the surface of the UCNPs, thermogravimetric analysis was performed using a thermogravimetric analyser coupled mass spectrometer (TGA-MS), Model TGA Q500 coupled Discovery MS (TA Instruments). These measurements were carried out in air (gas flux: 100 mL/min (10 mL/min He^+ 90 mL/min air)) at a heating rate of 10 °C/min.

Optical characterization. In order to determine the photoluminescence quantum yield (PLQY), dispersions of UCNPs in hexane were prepared with a UCNP concentration of 75 mg/mL. The PLQY of the samples was measured in a 1 mL quartz cuvette using a calibrated spectrofluorometer (Edinburgh Instruments, FLS920) equipped with an integrating sphere (Jobin-Yvon). A liquid nitrogen cooled NIR photon multiplier tube (PMT; Hamamatsu, R-5587) was used to measure the excitation beam, while a Peltier cooled extended red photomultiplier detector (Hamamatsu R2658P) was used to measure the visible emission. A 980 nm diode laser was applied as the excitation light source. The power at the focus of the laser beam was measured to be 43.8 mW, and the power density corresponded to 5.8 W/cm^2 (spot size: 0.754 mm^2). Absorption measurements were performed using the same UCNP dispersions and experimental setup, though recording the 980 nm intensity at the exit of the integrating sphere, rather than the upconversion emission. The PLQY has been calculated as the ratio of the emitted photons divided by the absorbed excitation photons (see Eq. 1 in the section Results and Discussion). The measurement followed a procedure which is described in more detail in the literature.[7, 8] In a first PLQY experiment, undoped reference samples of comparable size, phase and shape were used to account for possible inaccuracies related to absorption of the media (hexane) or scattering. However, no differences were observed when a second PLQY measurement was performed removing the reference sample and using the empty integration sphere instead, which is an observation consistent with previous studies.[9] Following these results, no reference sample was used for subsequent PLQY measurements.

For excitation power-dependent photoluminescence spectroscopy, a 980 nm monomode laser diode from Thorlabs (330 mW maximum excitation power) was used, and neutral density filters were added to reduce power below threshold. The beam was focused on the sample with a lens (5 cm focal distance, 2.5 cm diameter) and the luminescence was recorded with a fibre-coupled spectrophotometer from Avantes (Avaspec 2048L – USB2).

Lifetimes were measured using a 980 nm laser diode (CNI Opto-electronics Tech) as excitation source. Aiming for pulsed radiation, a chopper at 400Hz was inserted in the beam path. Then, the beam was focused on the sample, and it´s emission was collected with a 40x objective and a beam splitter (Thorlabs, BSS10) in backscattering mode. Light was directed to a monochromator (half-meter, Andor, Shamrock 500-i) equipped with a grating with 1200 lines/mm, and then recorded with a photomultiplier tube (Hamamatsu R928) connected to a 500MHz digital oscilloscope (LeCroy, WaveRunner LT342).

S3. ICP-OES Analysis

Table S2. Sodium and gadolinium ion concentrations in selected α- and β-$NaGdF_4$ UCNPs determined through ICP-OES measurements.

Host Material	**$[Na^+]$**	**$[Gd^{3+}]$**	**$[Na^+]$**	**$[Gd^{3+}]$**	**$[Na^+]/[Gd^{3+}]$**
α-$NaGdF_4$	51.09 mg/L	305.53 mg/L	2.22 mol/L	1.94 mol/L	1.14
	45.44 mg/L	343.66 mg/L	1.98 mol/L	2.19 mol/L	0.90
	66.46 mg/L	386.58 mg/L	2.89 mol/L	2.46 mol/L	1.18
	59.68 mg/L	337.87 mg/L	2.56 mol/L	2.15 mol/L	1.21
β-$NaGdF_4$	39.90 mg/L	267.13 mg/L	1.74 mol/L	1.70 mol/L	1.02
	13.99 mg/L	106.44 mg/L	0.61 mol/L	0.68 mol/L	0.90
	38.60 mg/L	278.37 mg/L	1.68 mol/L	1.77 mol/L	0.95

S4. Additional HRTEM Data

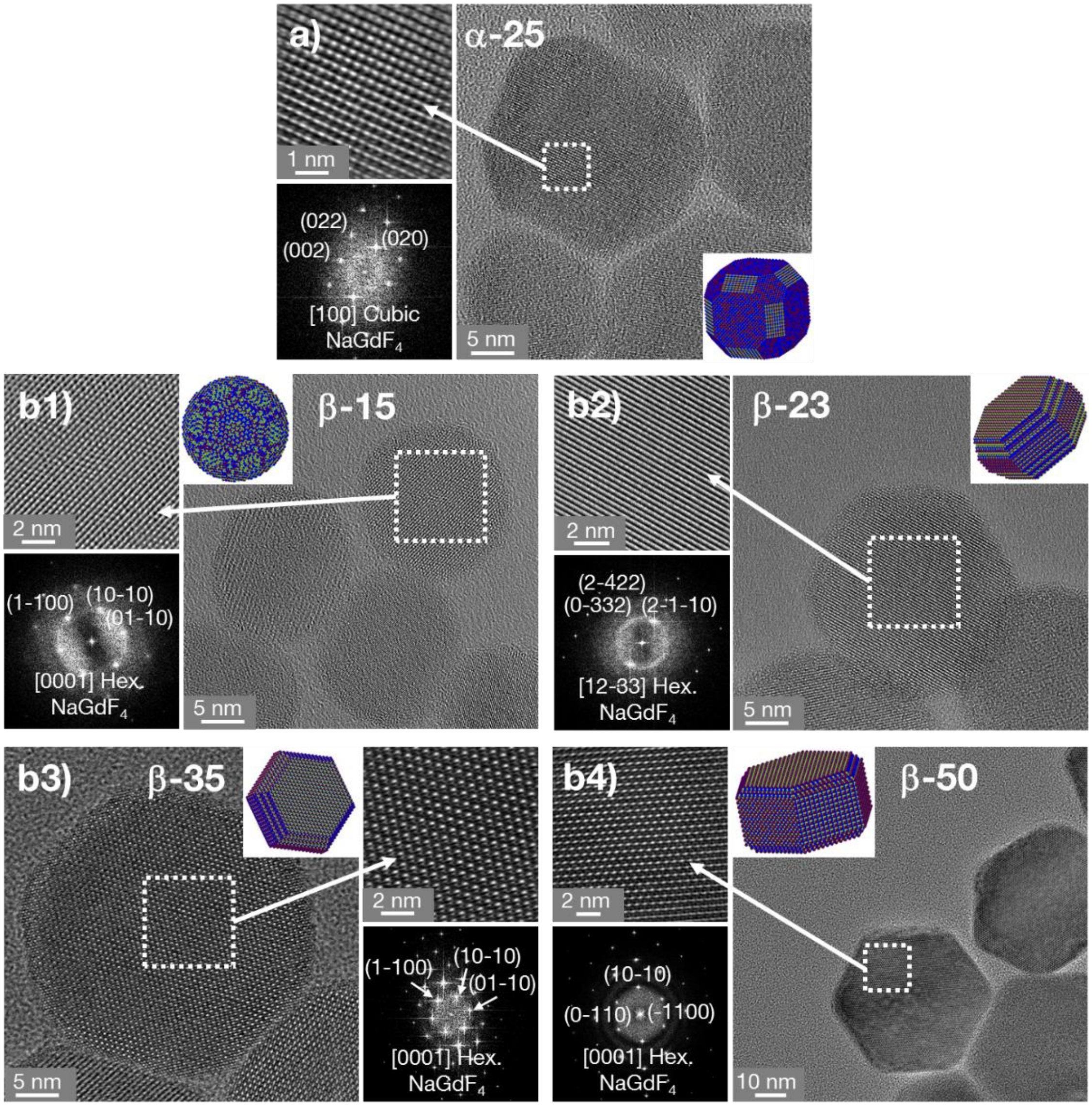

Figure S2. HRTEM images, SAED patterns and morphological models of (a) α- and (b) β-$NaGdF_4$:Er^{3+}/Yb^{3+} UCNPs.

S5. Volume and Surface of the Studied UCNPs

Table S3. Equations applied for the estimation of the surface area and volume for all observed morphologies.

Morphology	Surface (S)	Volume (V)	Scheme
Sphere	$4\pi r^2$	$\frac{4}{3}\pi r^3$	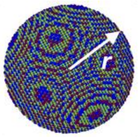
Hexagon	$3\sqrt{3}\,r^2+6rt$	$\frac{3}{2}\sqrt{3}\,r^2\,t$	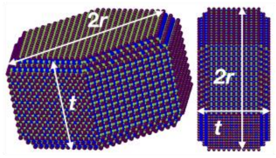
Truncated Cube	$24(d-t)^2+24\sqrt{2}\,t(d-t)$ $+4\sqrt{3}\,t^2$	$8(d-t)^3+24t(d-t)^2$ $+12t^2(d-t)+\frac{4}{3}t^3$	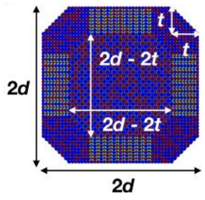

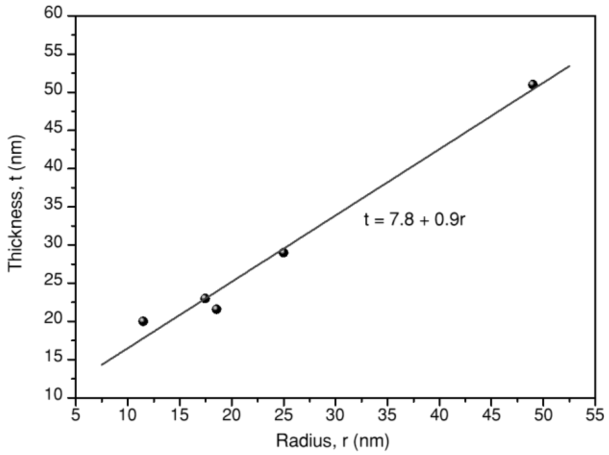

Figure S3. Relationship between the radius, r, and the thickness, t, of the obtained hexagonal plates. Dots are the experimental data, while the line represents the linear fit, expressed by the shown equation.

S6. Power-Dependent Photoluminescence

The number, *n*, of excitation photons required to generate an upconverted photon leaves a clear signature on the relationship between emission intensity, *I*, and excitation power, *P*. In a situation, in which the probability of upconversion is low compared to the probability of spontaneous emission to a lower state, this relationship can be defined by $I \sim P^n$. Thus, for the case of Er^{3+}/Yb^{3+} co-doped systems, in which the upconversion process generating both the green and red emissions require two steps and therefore needs two excitation photons, a quadratic relationship between the intensity of these emissions and the excitation power is expected. However, as mentioned, this is only true if the probability of upconversion is low. If for an intermediate state the probability of losing an electron following an upconversion process can compete with the probability of spontaneous emission, the mentioned relationship may change. Particularly, it becomes $I \sim P^m$ where *m* is smaller than *n*. The exact value of *m* depends on the probability of the upconversion process compared to spontaneous emission, but also on the nature of the upconversion scheme (whether it is based on energy transfer, on energy state absorption or on both).[10] Accordingly, it is not constant for all excitation powers and it may change with the crystal host. Indeed, this lowering of the exponent is common in UCNPs based on fluorides, where upconversion processes are favoured, and is often regarded to as “saturation”.[11]

For a fair comparison between host materials, it is important to clarify whether the excitation power applied is high enough to enter a saturated regime, and if so, how the different host materials differ in that sense. Figure S4 shows the results obtained after measuring the green and red emission intensities of several samples at different excitation powers. It must be noted that the excitation power density applied for PLQY measurements all along this study was 5.8 W/cm^2 which is in the lower range of power considered in Figure S4. The obtained data in Figure S4 were fit to straight lines (please, note that a logarithmic scale is being used) to determine the value of *m*. In each case, two fits are used. One is using the first five data points as reference and one is using the five last data points as reference. In this way, a lowering of *m*, if it exists, would become clear.

The general conclusion obtained from the figure is that $m = n = 2$ for most of the cases, at least for the excitation power used for PLQY measurements. This means that PLQY experiments were performed out of the saturation range.

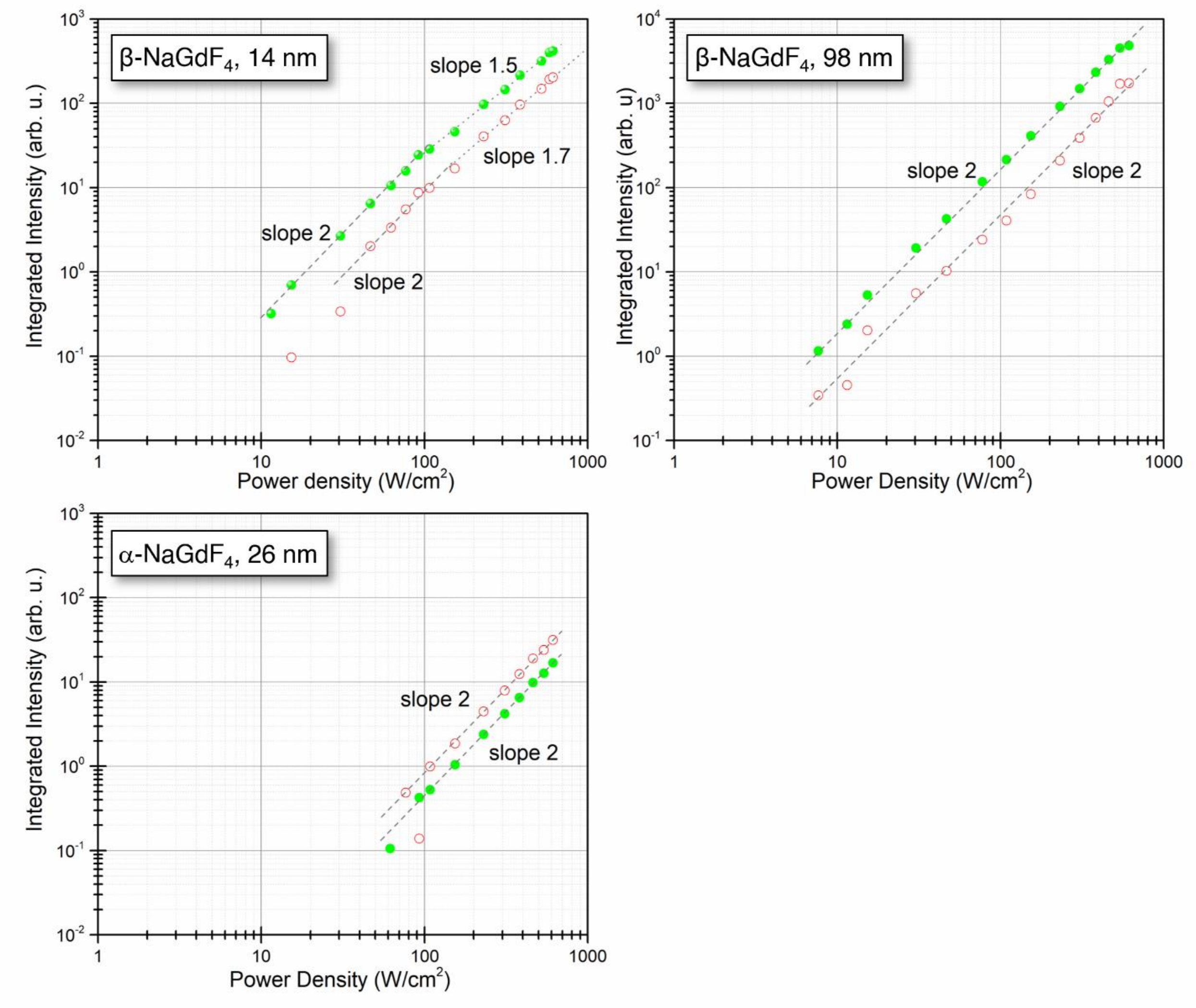

Figure S4. Intensity versus excitation power of the green (full green circles) and red (red empty circles) emission bands measured for oleate-capped Er^{3+}/Yb^{3+} co-doped UCNPs in hexane. The first and last five values were fit to straight lines (dashed grey lines) to visualize the degree of saturation in each case.

S7. Absorption and PLQY of the UCNPs

Table S4. Absorption measured for the studied UCNPs. Each sample has been measured twice. The systematic error of the absorption measurements is 5 %. The measured PLQY is also given for each sample, with the subindex G for the green and R for the red emission, respectively.

Sample	β-14	β -15	β -23	β -35	β -37	β -50	β -98
Abs%	18	8	2	19	15	10	10
$PLQY_G$ ($x10^{-2}$ %)	0.4 ± 0.1	0.51 ± 0.01	1.3 ± 0.3	8 ± 2	14.9 ± 0.2	8 ± 3	68 ± 1
$PLQY_R$ ($x10^{-2}$ %)	0.15 ± 0.08	0.08 ± 0.01	0.6 ± 0.3	2.4 ± 1	4.0 ± 0.2	3 ± 2	37 ± 1

Sample	α-15	α-22	α-26	α-29
Abs%	6	17	17	10
$PLQY_G$ ($x10^{-2}$ %)	0.7 ± 0.3	0.7 ± 0.2	0.16 ± 0.01	0.2 ± 0.1
$PLQY_R$ ($x10^{-2}$ %)	2.9 ± 0.1	2.3 ± 1	0.8 ± 0.1	1.5 ± 0.1

S8. Assessment of Potential Laser-induced Thermal Effects

When a nanoparticle is excited with light, it may happen that its temperature or the temperature of the environment (hexane in the case of this study) increases. If so, the efficiency of this heating depends on the excitation power, on the thermal properties and on the absorption coefficient of the host material as well as the solvent. Moreover, non-radiative relaxations, if intense, could also induce temperature fluctuation. In this section, we pay attention to possible thermal changes that may affect the results discussed in the main manuscript.

In order to measure the temperature of a system that is based on Er^{3+}-doped UCNPs, the green emission due to Er^{3+} can be used. It is composed by the emission associated to two different transitions: $^2H_{11/2} \rightarrow {}^4I_{15/2}$, at around 530 nm, and $^4S_{3/2} \rightarrow {}^4I_{15/2}$, at around 550 nm. As both excited states, $^2H_{11/2}$ and $^4S_{3/2}$, are energetically close to each other, their electronic population is shared and distributed between them following a Boltzmann function:[12]

$$\frac{I_H}{I_S} = B\, exp\left(-\frac{\Delta E}{k_B T}\right) \tag{ES1}$$

In this expression, ΔE is the energy separation between the $^2H_{11/2}$ and $^4S_{3/2}$ states, T is the temperature, k_B is the Boltzmann's constant and B is a constant that depends on the degeneracies and spontaneous emission rates of both states.[13] It is clear from the equation that the intensity ratio between these two green emissions changes with temperature. Indeed, Er^{3+}-doped materials have been often proposed as remote optical sensors of temperature thanks to this property,[12] which will be exploited here to investigate potential thermal effects upon laser excitation.

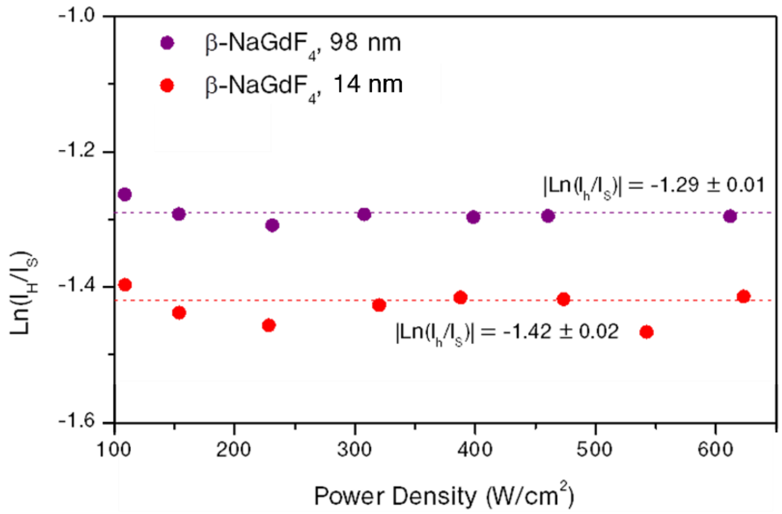

Figure S5. Intensity ratio of Er^{3+} green emissions plotted versus excitation power density in three different sets of UCNPs.

Figure S5 shows how the logarithm of the intensity ratio between the areas of both green emission bands changes with excitation power. Rather than using the ratio, the logarithm of the ratio has been used since the expression given in equation ES1 is exponential. Thus, a logarithmic representation makes interpretations straight forward and values are easy to compare with those from other publications. For these types of UCNPs, a thermal change of one degree in the material is considered normal and implies changes in Ln(I_H/I_S) of around 0.02 units. Higher temperatures produce higher values of Ln(I_H/I_S).[14, 15] Thus, as no ascending trend of Ln(I_H/I_S) was observed with increasing excitation power (Figure S5), we can conclude that heat generation is negligible within the studied excitation power range. To support this conclusion, the average value and the standard deviation of the obtained data have been calculated (values shown in Figure S5), revealing an error of less of 1 °C.

S9. $NaGdF_4$ compared to $LiYF_4$ and $NaYF_4$

Considering the many factors that affect PLQY, we framed the obtained results in context of two additional popular upconversion host materials, $LiYF_4$ and $NaYF_4$. Therefore, and to provide a more general picture on upconversion PLQY, oleate-capped Er^{3+}/Yb^{3+} co-doped $LiYF_4$ (tetragonal crystal structure) and $NaYF_4$ (cubic crystal structure) nanoparticles were synthesised and their PLQY was measured under the same conditions as for the $NaGdF_4$ series. TEM images of the obtained UCNPs, their XRD patterns and corresponding PLQY values are summarised in Figure S6. As each host material exhibited a specific shape, the S/V ratios are also shown (Figure S6d). To allow for comparison, selected $NaGdF_4$ results obtained for samples with comparable S/V values were included in the plot. As a general trend, smaller S/V ratios were linked to larger PLQY values. However, given the very different size and shape of these $LiYF_4$- and $NaYF_4$-based UCNPs, as well as a differentiated crystal lattice, deduction of any general rules from this comparison must be taken with care.

An additional consequence of changing the host material is that, besides green and red emissions, also the blue emission band linked to the $^2H_{9/2} \rightarrow {}^4I_{15/2}$ Er^{3+} transition is observed for some of the investigated UCNPs. The determined PLQY value for this blue upconversion emission was logically smaller than those obtained for red and green emissions, as this is typically a weak emission. More precisely, PLQY values of 0.023% for $LiYF_4$, 0.012% for β-$NaGdF_4$ (S/V = 0.086) and 0.0015% for α-$NaYF_4$ were obtained.

All together, we can see that there is a dependency on size that goes beyond surface quenching when the nanoscale is approached. The increase of the surface area over the volume as particles become smaller is undoubtedly one of the major effects to consider, but a careful analysis also requires including shape differentiation and lattice distortion, being the relevance of this last option on the crystal phase under study. A technologically relevant consequence of our findings is that PLQY of Er^{3+},Yb^{3+}-doped α-$NaGdF_4$ surpassed that of β-$NaGdF_4$ for particle sizes below 20 nm. This fact was particularly outstanding for the red upconversion emission, that became an order of magnitude higher for α-$NaGdF_4:Er^{3+},Yb^{3+}$ than for β-$NaGdF_4:Er^{3+},Yb^{3+}$ when the UCNPs reached the critically small enough size of 15 nm.

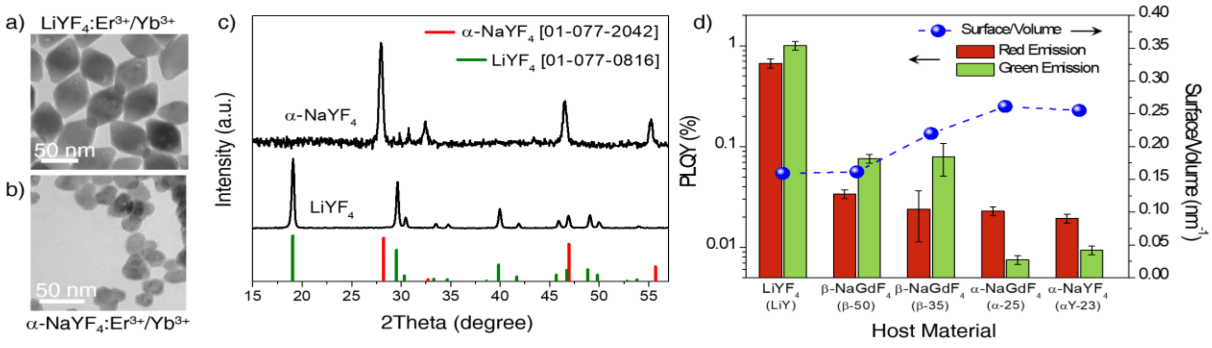

Figure S6. TEM micrographs of a) $LiYF_4:Er^{3+},Yb^{3+}$ and b) α-$NaYF_4:Er^{3+},Yb^{3+}$ UCNPs. c) XRD diffractograms measured for both samples, together with the respective reference patterns. d) Green and red PLQY values measured (bars) and S/V ratio calculated for each sample (blue dots). To facilitate comparison, $NaGdF_4$ PLQY values of samples with comparable S/V values are included in the plot.

S10. Effect of Oleate Surface Groups on PLQY

FTIR spectroscopy. The FTIR spectrum obtained on a representative sample of oleate-capped UCNPs (Figure S7) shows characteristic peaks that can clearly be assigned to the oleate capping ligands on the UCNP surface. Particularly, the peaks at 2924 cm^{-1} and 2853 cm^{-1} are assigned to the asymmetric and symmetric stretching of -CH$_2$ groups while the peaks at 1557 cm^{-1} and 1460 cm^{-1} originate from the asymmetric (δ_{as}) and symmetric (δ_s) -COO$^-$ stretching.[16] The presence of water and hydroxyl groups originating most likely from the atmospheric moisture taken up during FTIR sample preparation and measurement is obvious from the broad band observed at 3450 cm^{-1} and the peak at 1640 cm^{-1}.

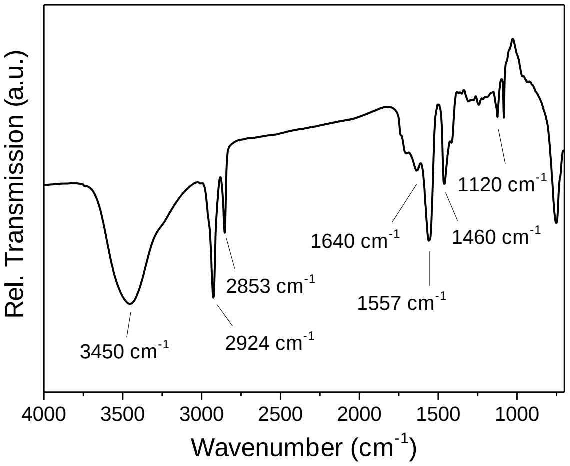

Figure S7. Representative FTIR spectrum of oleate-capped β-NaGdF$_4$:Er^{3+}/Yb^{3+} UCNPs.

Oleate density on the UCNP surface. In order to address the question to what extent the surface modification plays a role for PLQY variation within the investigated set of UCNPs, the amount of oleate (OA) in each sample and the degree of surface modification or OA density (*density* refers here to the amount of OA normalized to the UNCPs' surface) have been determined. This provides information on whether the surfactant is found equally on each type of UCNP, regardless of size and shape, or, on the contrary, whether the surface of the different UCNPs is not equivalent leading to a size and morphology dependent OA density. If the latter is the case, higher OA density may provide a larger number in potential quenchers ultimately contributing to size and morphology dependent PLQY variation. For clarification, TG measurements were carried out for all samples allowing for the determination of the amount of OA and a subsequent estimation of the OA density on the UCNP surface. The obtained TGA curves showing the mass loss upon heating of the samples are given in Figure S8.

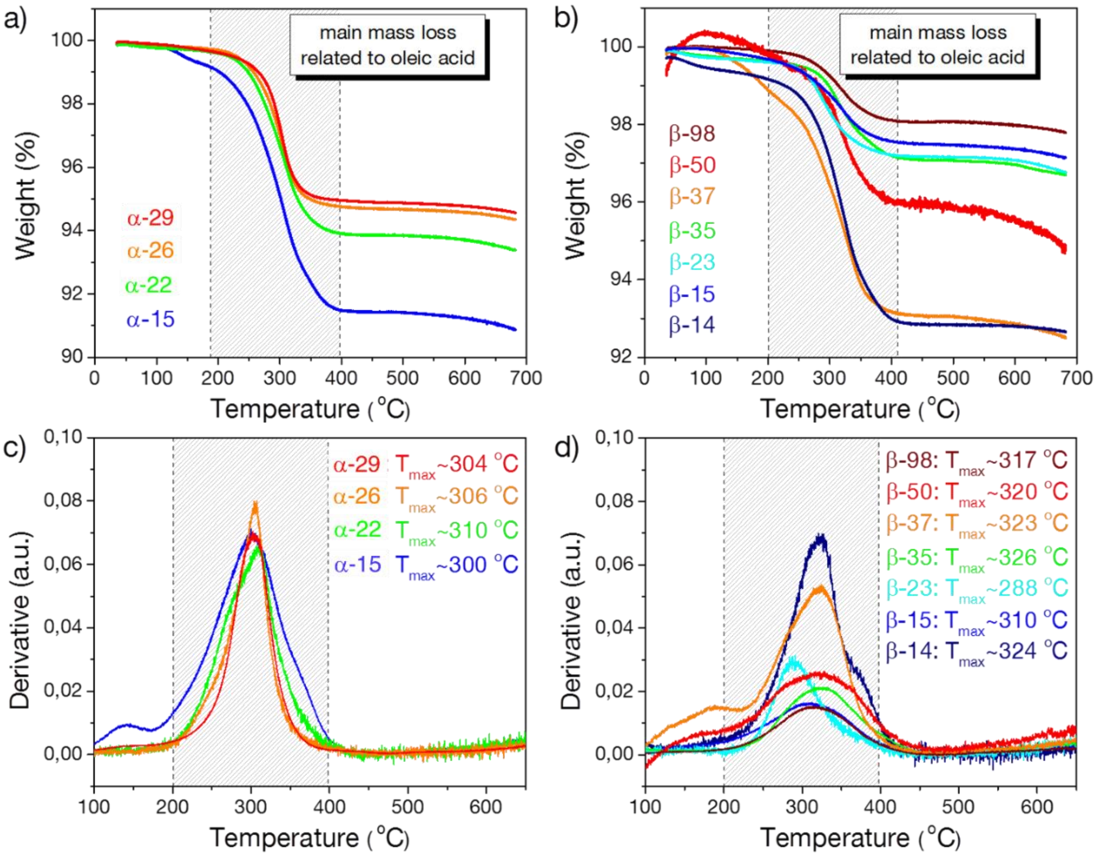

Figure S8. TGA curves obtained upon heating oleate-capped Er^{3+}/Yb^{3+} doped $NaGdF_4$. (a) α-phase samples, (b) β-phase samples. Derivative of the weight loss as function of temperature for oleate-capped (c) α- and (d) β-$NaGdF_4$:Er^{3+}/Yb^{3+} UCNPs.

The overall observed small mass loss at around 100 °C is attributed to atmospheric moisture, followed by the main mass loss starting from approximately 200 °C and ranging from 2 to 6% for β-phase UCNPs as well as from 4 to 8% for α-phase UCNPs. The maximum decomposition temperatures were determined through the first derivatives of the TGA curves revealing values in the range from 290 to 325 °C (Figure S8c and d). This major decomposition step is assigned to the decomposition of the organic OA surfactant.[16] No further mass loss is observed at temperature higher than 400 °C, and it can be assumed that the remaining mass is only related to $NaGdF_4$.

In order to compare the number of potential quenchers on the UCNP surface as a function of the particle morphology, the OA density has to be estimated. Therefore, the following equation was used in order to calculate the mass density of hexagonal β-$NaGdF_4$ doped with 2 mol% Er^{3+} and 20 mol% Yb^{3+}:[17]

$$\rho_{hexagonal} = \frac{m}{V} = \frac{M\,N'_{hexagonal}}{N_A \frac{\sqrt{3}}{2} c\, a^2} \qquad \text{(ES2)}$$

Herein, m is the mass and V the volume, which can be expressed by the molecular mass M of $NaGd_{0.78}Yb_{0.2}Er_{0.02}F_4$ (M = 259.59 g mol^{-1}), N' is the number of $NaGd_{0.78}Yb_{0.2}Er_{0.02}F_4$ units in one crystal cell ($N'_{hexagonal}$ = 1.5), N_A is the Avogadro constant ($N_A = 6.022 \cdot 10^{23}$ mol^{-1}), and a and c are the respective hexagonal lattice parameters.

The mass density of the equivalent cubic α-NaGdF$_4$ host material was calculated using:

$$\rho_{cubic} = \frac{m}{V} = \frac{M\, N\prime_{cubic}}{N_A\, a^3} \qquad \text{(ES3)}$$

with $N'_{\text{cubic}} = 2$ and a being the cubic lattice parameter.

Using the lattice parameters obtained from fitting our XRD pattern, the material's density as a function of S/V can be determined for the α- and β-UCNPs. Results are shown in Figure S9. As observed, there´s a smooth trend in the values, that are slightly different from the standard ones (ρ(α-NaGdF$_4$) = 5.06 g cm^{-3}, ρ(β-NaGdF$_4$) = 5.65 g cm^{-3}), which would appear at S/V tending to zero (large particles).

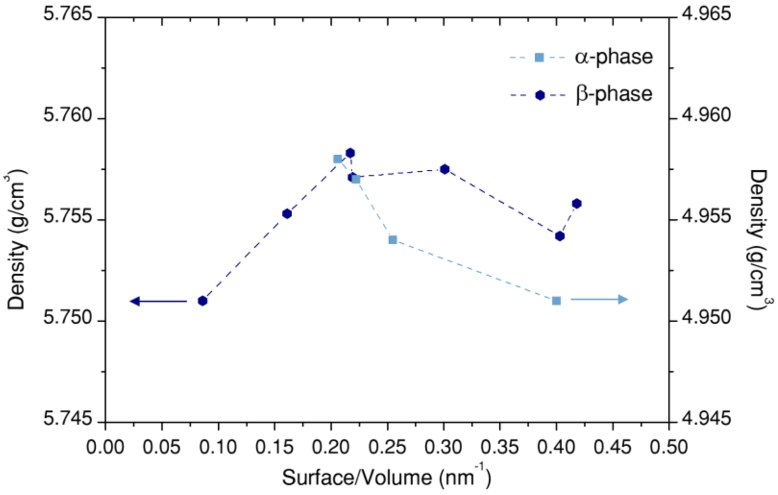

Figure S9. Calculated mass densities of the α- as well as β-phase samples as a function of S/V. For comparison, standard values are: ρ(α-NaGdF$_4$) = 5.06 g cm^{-3}, ρ (β-NaGdF$_4$) = 5.65 g cm^{-3}.

Subsequently, with the help of these densities and the characteristic volume of each UCNP type, the number of particles, N, present in the sample was estimated. The OA density was defined as (M_{OA}/N)/S, where M_{OA} is the calculated mass of OA and S the surface area of the UCNPs. The as-determined OA density on the surface of each investigated sample is presented in Figure S10. As shown, the two repetitions of the measurement produce almost the same results, which indicates good reproducibility. It is further clear from Figure S10 that the OA density varies from sample to sample. However, no specific trend could be identified for the β-phase UCNPs. Instead, in general lower OA densities were obtained for the α-phase UCNPs with increasing S/V.

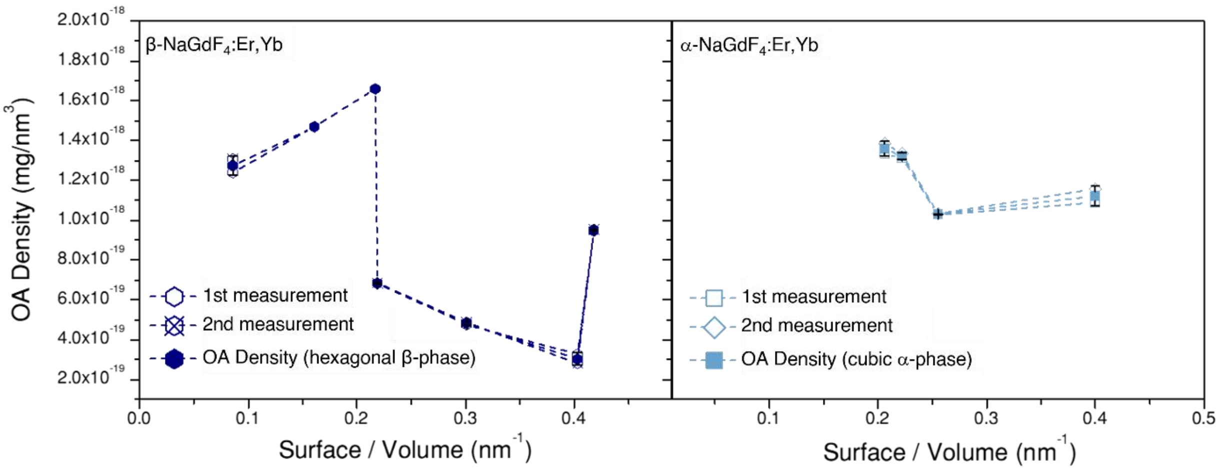

Figure S10. Estimated OA densities on the surface of Er^{3+}/Yb^{3+} co-doped α- and β-NaGdF$_4$ UCNPs.

It seems intuitive to correlate larger OA densities with more severe luminescence quenching. However, we do not know *a priori* how significant the variation in OA density must be to trigger a measurable difference in PLQY. Aiming to clarify if the observed differences in OA density should be taken into account in our PLQY study, we compared the data sets obtained for the PLQY (Figure 4, main text) with Figure S10. In case of α-phase UCNPs, the OA density decreased from S/V ~ 0.2 to 0.4 nm. Taking into account that a higher OA density is expected to result in more pronounced photoluminescence quenching and therefore lower PLQY, this trend would be in agreement with the PLQY data for the α-phase (Figure 4b, main text). However, there is no correlation between the larger differences in OA density in the case of β-phase and the measured PLQY trend (Figure 4a, main text). In particular, the observed discontinuities in the OA density don´t appear in PLQY. Thus, although OA density is not the same in every sample, it seems that overall, the measured fluctuations are too small to produce a relevant influence on the PLQY. This means that the main contribution of OA as a quenching agent affects almost equally the surfaces of all considered UCNP samples, and it is suggested that the size and morphology dependent variation of OA density is not significant enough to explain the overserved PLQY variation.

S11. Interionic Distance and its Influence on PLQY

Förster-Dexter theory in the dipole-dipole approximation shows that the energy transfer probability, W_{Tr}, can be defined as:[18]

$$W_{Tr} = \frac{C_{DA}}{R^6} \rightarrow \frac{W_{Tr}}{W_f} = \left(\frac{R_f}{R}\right)^6 \tag{ES4}$$

where C_{DA} is the energy transfer microparameter and is defined as:[18]

$$C_{DA} = \frac{3\hbar^4 c^4}{4\pi n^4}\frac{Q_A}{\tau_0}\int \frac{L_D(E)\cdot L_A(E)}{E^4} dE \tag{ES5}$$

In this definition, n is the refractive index, Q_A the absorption cross-section of the acceptor (Er^{3+} ions, in case of this study), τ_0 is the intrinsic radiative lifetime, L_i is the normalized line shape of the acceptor absorption ($i = A$, *i.e.* Er^{3+}) and donor emission ($i = D$, *i.e.* Yb^{3+}), and E is the energy of the transitions. Therefore, the integral represents the overlap between the absorption of the acceptor and the emission of the donor.

Equation (ES4) can be written in a differential form, dividing W_{Tr} by the probability of energy transfer after a lattice deformation, W_f, that is defined by an interionic distance R_f. This is how the relationship on the right side of equation (ES4) is obtained. However, to write this expression it has been assumed that the microparameter C_{DA} remains constant before and after the deformation, which is not necessarily true, as shown below. Nevertheless, in a first approximation it can be considered as constant.

Equation (ES4) allows to estimate how the probability of the process will be influenced by a certain Ln^{3+}-Ln^{3+} distance variation. To do so, it must be noted that upconversion is a multistep process, and for the population of either the green or the red emitting levels two subsequent $Yb^{3+} \rightarrow Er^{3+}$ energy transfer processes constitute the complete upconversion mechanism (Figure 3a of the main text). Therefore, following the basic rules of probability, the total probability of the process will be related to the square of the probability of one single process. Then, approximating the volume of the unit cell as R^3 (which is an equivalent of using an averaged distortion of lattice parameters c and a in the case of the hexagonal lattice, but doesn't involve any approximation for the cubic phase), a maximum increase in upconversion probability of 2 % in the case of the β-phase and around 3 % in the case of the α-phase due to changes in the interionic distance were estimated from equation (ES4). If translated to the measurements shown in Figure 4 of the main paper, these values are too small to justify the trends observed.

We can now reconsider the possible changes that C_{DA} can undergo due to the lattice deformation. The considered lattice modifications can have an effect on the spectral lines, yet lanthanides are not very sensitive to these and thus, the overlap integral and Q_A are not expected to change significantly. However, the refractive index can change, as it is intimately related to the density of the material. In a simplified model, the volume of the unit cell and the refractive index can be described with Clausius-Mossotti equation, that, in its differential form, is:[19]

$$\frac{\Delta V}{V} = -\frac{6n}{(n^2-1)(n^2+2)}\Delta n \tag{ES6}$$

This means that when the density of the material increases, as it happens when the unit cell is contracted, the refractive index increases as well, and *vice versa*. According to equation (ES5), the dependence of C_{DA}

with n follows a n^{-4} law, implying that its effect is thus the opposite of the previous one based on interionic distance. This happens here since R and n variations are both due to a change in the volume of the lattice, and its consequence is that the previous estimation, which considered only distances, is overestimated. Since this previous estimation was already small to justify PLQY variations in Figure 4, and now it is further decreasing, it can be assumed that variation in energy transfer probabilities linked to changes in the crystal lattice are not a major parameter to consider in this study. Still, for the sake of completeness, this overestimation was assessed. In order to do so, the value of n in equation (ES6) was introduced and approximated as ~1.5 (the refractive index of $NaYF_4$).[20] Then, using the maximum and minimum values obtained for the volume of the unit cell in each crystal phase (Figure 6 of the main paper), a refractive index variation, Δn, can be calculated. This led to $\Delta n = 0.002$ for the α-phase and $\Delta n = 0.001$ for the β-phase, which gives a C_{DA} decrease of 0.6 % in the former and of 0.3 % in the latter case, respectively. Even considering that there are two energy transfer steps in each UC process, these numbers are significantly smaller than the contribution related to the distance between Ln^{3+} (2% and 3%, respectively), which, as mentioned above, was not enough to justify the observed PLQY variations.

S12. Rietveld Refinement

The XRD diffractograms measured for each sample were analysed using FullProf Suite software. As Crystallography Information Files (CIF) are not available for $NaGdF_4$, those of $NaYF_4$ were used, modified to exchange Y by Gd. As all the series have been analysed following the same protocol, consistency between results is warrantied. Peaks have been modelled using a pseudo-Voigt function over 10 to 80° for the beta phase, and 10° to 65° for the alpha phase. The fitting routine was performed starting with the scale factor and two (out of six) background parameters, followed by the lattice constants. Subsequently, atomic positions and the different peak shape parameters were sequentially fit, readjusting at this point the scale factor. Following this step, the background was further refined and the routine was repeated, searching for a minimum. At the end, the overall thermal parameter was fit. Asymmetry parameters and atoms occupancy were not considered.

The fit has been repeated twice to ensure consistency of results and to provide a standard deviation. During the fit, instrument corrections are considered constant, as the instrument used was always the same. In each case, the obtained χ^2 was below 1.5. Examples of the obtained fit are shown in Figure S11.

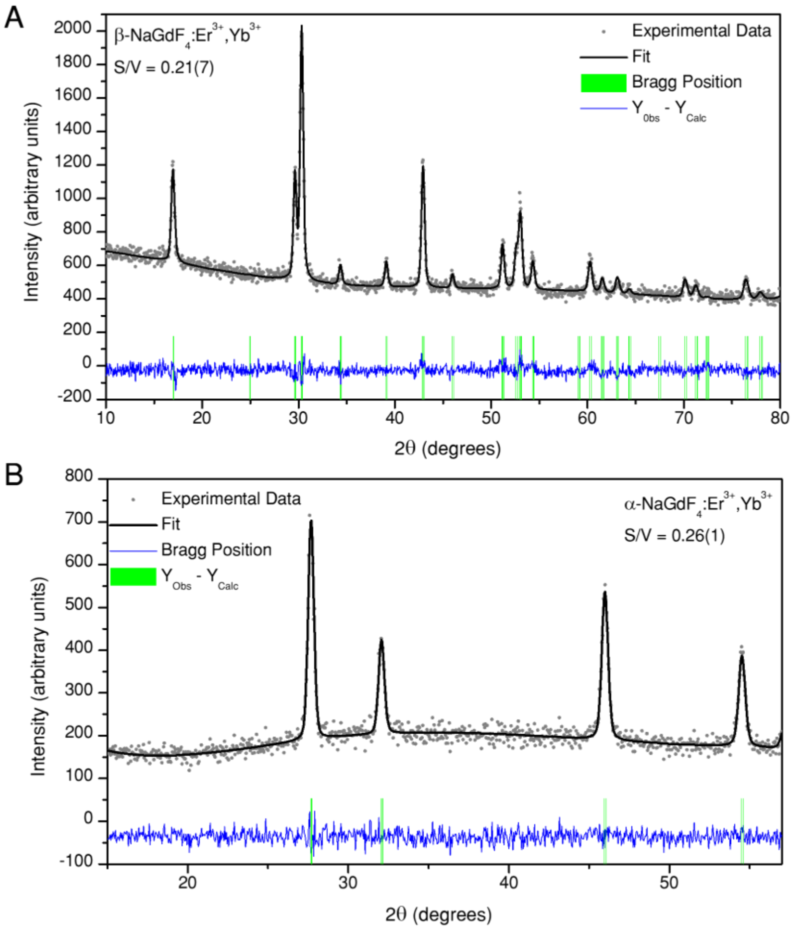

Figure S11. Examples of Rietveld refinement for each type of sample, β-$NaGdF_4$ (A) and α-$NaGdF_4$ (B). The plots show experimental data (grey dots), the fit (black line), the calculated positions for Bragg reflections (green bars) and the result of subtracting the calculated values from the measured data (blue line).

S13. Scherrer Parameter and Strain

The Scherrer formula relates the half-width of XRD reflections, β_{hkl}, with the crystallite size, D:

$$\beta_{hkl} = \frac{K\,\lambda}{D\,cos\theta} \tag{ES6}$$

Where θ is the diffraction angle (in rad), λ the X-Ray wavelength and *K* is the Scherrer parameter. This *K* parameter takes values close to unity, and is thus often assumed as 1. However, *K* depends on the direction inside the crystal through the Miller indices *h k l* and on the exact geometrical shape of the crystallite. As often crystallites are irregular in shape, being accurate in the definition of *K* doesn´t seem possible. However, in the present case the geometry of the nanoparticles was well-defined, and they can be assumed as formed by one single crystallite (otherwise, when calculated, D will reveal that this assumption is wrong). Accordingly, it was possible to further refine D through the accurate definition of *K*.

In the simpler case of a cubic lattice, *K* is 1.0747 if the crystallite is a sphere. If it is a cube, it can be calculated for each *h k l* using the formula:[21]

$$K = \frac{6h^3}{N\cdot[6h^2-2(k+l)+kl]} \tag{ES7}$$

with N = $\sqrt{h^2+k^2+l^2}$.

For non-cubic lattices, equivalent formulas exist, but the Miller indexes cannot be used directly. However, the exact values are tabulated in papers specifically devoted to this subject. If a crystallite with hexagonal lattice is spherical, *K* is 1.20. In the case of hexagonal plates, *K* takes values that depend on the exact dimensions of the hexagon, and have to be calculated for each case following the manuscripts on the subject.[22] Considering these values, it is possible to determine the strain and the crystallite size using the Williamson-Hall equation (Eq. 4, main manuscript). In order to do so, linear fits were calculated from the breadth and 2Θ values obtained in the Rietveld refinements (Figure S12). While the intercept of the fit is directly related to D, the slope is related to the strain.

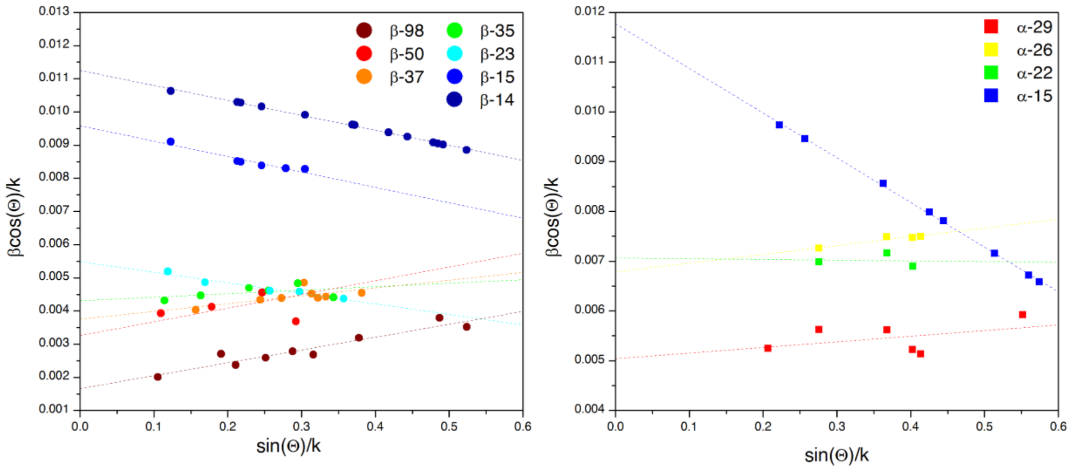

Figure S12. Fits performed to calculate ε and D, following the Williamson-Hall equation (Eq. 4, main manuscript).

S14. Additional Host-Related Parameters Influencing PLQY

In both α- and β-$NaGdF_4$, the dopants Er^{3+} and Yb^{3+} enter the lattice substituting the Gd^{3+} ions. This can induce some distortion of the lattice due to the different ionic radii of the Ln^{3+} ions incorporated (Er^{3+} and Yb^{3+}) and Gd^{3+}. In contrast, the generation of defects linked to charge compensation, such as vacancies, is not expected since all ions are trivalent (Ln^{3+}). Some emission characteristics (including relative intensities (branching ratios), level splitting, peak width and spectral line-shape) can change from host to host for several reasons beyond the effect of substitutional doping. Table S5 summarizes some parameters relevant in this context.

Table S5. Summary of the properties of α- and β-$NaGdF_4$, including the energy of the highest phonon, the lattice parameters calculated for each sample by fitting the XRD patterns in **Figure 1**, the symmetry of the Gd^{3+} sites, respectively, in the undoped material, and the symmetry of the same position in the lattice upon occupation by the Ln^{3+} dopant. To the best of our knowledge, no data exist for the highest energy phonon of α-$NaGdF_4$.

Host	Symmetry		Lattice Parameters (Å)	High Energy Phonon (cm^{-1})	Ref.
	Gd^{3+}	Ln^{3+}			
α-$NaGdF_4$	O_h	C_s or C_2	*a* = 5.577	-	23
β-$NaGdF_4$	C_{3h}	C_{3h} or C_1	*a* = 6.024 *c* = 3.567	~450	23-25

S15. References

1. N. Bogdan, F. Vetrone, G. A. Ozin and J. A. Capobianco, *Nano Lett.*, 2011, **11**, 835.
2. F. Vetrone, R. Naccache, V. Mahalingam, C. G. Morgan and J. A. Capobianco, *Adv. Funct. Mater.*, 2009, **19**, 2924.
3. H. X. Mai, Y. W. Zhang, R. Si, Z. G. Yan, L. D. Sun, L. P. You and C. H. Yan, *J. Am. Chem. Soc.*, 2006, **128**, 6426.
4. S. Bernal, F. J. Botana, J. J. Calvino, C. Lopez-Cartes, J. A. Perez-Omil and J. M. Rodriguez-Izquierdo, *Ultramicroscopy*, 1998, **72**, 135.
5. V. Grillo and E. Rotunno, *Ultramicroscopy*, 2013, **125**, 97.
6. V. Grillo and E. Rotunno, *Ultramicroscopy*, 2013, **125**, 112.
7. S. K. W. MacDougall, A. Ivaturi, J. Marques-Hueso and B. S. Richards, *Rev. Sci. Instrum.*, 2014, **85**, 063109.
8. C. Würth, M. Grabolle, J. Pauli, M. Spieles and U. Resch-Genger, *Nat. Protoc.*, 2013, **8**, 1535
9. J. C. Boyer and F. van Veggel, *Nanoscale*, 2010, **2**, 1417.
10. M. Pollnau, D. R. Gamelin, S. R. Lüthi, H. U. Güdel and M. P. Hehlen, *Phys. Rev. B*, 2000, **61**, 3337.
11. M. Quintanilla, I. X. Cantarelli, M. Pedroni, A. Speghini and F. Vetrone, *J. Mater. Chem. C,* 2015, **3**, 3108.
12. V. K. Rai, *Appl. Phys. B*, 2007, **88**, 297.
13. M. Quintanilla, E. Cantelar, F. Cussó, M. Villegas and A. C. Caballero, *Appl. Phys. Express*, 2011, **4**, 022601.
14. E. Hemmer, M. Quintanilla, F. Légaré and F. Vetrone, *Chem. Mater.*, 2015, **27**, 235.
15. F. Vetrone, R. Naccache, A. Zamarron, A. J. de la Fuente, F. Sanz-Rodriguez, L. M. Maestro, E. M. Rodriguez, D. Jaque, J. G. Sole and J. A. Capobianco, *ACS Nano*, 2010, **4**, 3254.
16. L. Zhang, R. He and H.-C. Gu, *Appl. Surf. Sci.*, 2006, **253**, 2611.
17. F. Zhang, *Photon Upconversion Nanomaterials*, Springer-Verlag, Berlin, Heidelberg, 2015.
18. D. L. Dexter, *J. Chem. Phys.*, 1953, **21**, 836.
19. J. Burghoff, S. Nolte and A. Tünnermann, *Appl. Phys. A: Mater. Sci. Proc.*, 2007, **89**, 127.
20. B. Herter, S. Wolf, S. Fisher, M. Peters, B. Bläsi and J. C. Goldschmidt, Brussels, Belgium, 2012.
21. J. I. Langford and A. J. C. Wilson, *J. Appl. Crystallogr.*, 1978, **11**, 102.
22. S. Lele and T. R. Anantharaman, *Proc. Indian Academy of Sciences - Section A*, 1966, **64**, 261.
23. D. Tu, Y. Liu, H. Zhu, R. Li, L. Liu and X. Chen, *Angew. Chem.*, 2013, **125**, 1166.
24. A. Aebischer, M. Hostettler, J. Hauser, K. W. Krämer, T. Weber, H. U. Güdel and H.-B. Bürgi, *Angew. Chem. Inter. Ed.*, 2006, **45**, 2802.
25. M. M. Lage, R. L. Moreira, F. M. Matinaga and J. Y. Gesland, *Chem. Mater.*, 2005, **17**, 4523.
26. C. Görller-Walrand, K. Binnemans and L. Fluyt, *J. Phys.: Cond. Matter*, 1993, **5**, 8359.
27. D. T. Tu, W. Zheng and X. Y. Chen, *Angew. Chem. Inter. Ed.*, 2015, **54**, 1077.
28. M. Karbowiak, J. Cichos and C. Rudowicz, *Angew. Chem. Inter. Ed.*, 2015, **54**, 1074.
29. C. Renero-Lecuna, R. Martín-Rodríguez, R. Valiente, J. González, F. Rodríguez, K. W. Krämer and H. U. Güdel, *Chem. Mater.*, 2011, **23**, 3442.
30. P. Boutinaud, R. Mahiou, N. Martin and M. Malinowski, *J. Lumin.*, 1997, **72–74**, 809.
31. J. L. Sommerdijk, *J. Lumin.*, 1973, **6**, 61.
32. A. Meijerink, G. Blasse, J. Sytsma, C. de Mello Donega and A. Ellens, *Acta Phys. Pol.*, 1996, **90**, 109.